Monthly Notices of the ROYAL ASTRONOMICAL SOCIETY

MNRAS **503,** 2444–2456 (2021) doi:10.1093/mnras/stab642
Advance Access publication 2021 March 5

The effect of a solar flare on chromospheric oscillations

David C. L. Millar [1]★ Lyndsay Fletcher [1,2] and Ryan O. Milligan [1,3]

[1]*School of Physics & Astronomy, University of Glasgow, Glasgow G12 8QQ, UK*
[2]*Rosseland Centre for Solar Physics, University of Oslo, PO Box 1029 Blindern, NO-0315 Oslo, Norway*
[3]*Astrophysics Research Centre, School of Mathematics and Physics, Queen's University, Belfast BT7 1NN, Northern Ireland, UK*

Accepted 2021 March 1. Received 2020 December 19; in original form 2020 July 21

ABSTRACT

Oscillations in the solar atmosphere have long been observed both in quiet conditions and during solar flares. The chromosphere is known for its 3-min signals, which are strong over sunspot umbrae, and have periods determined by the chromosphere's acoustic cut-off frequency. A small number of observations have shown the chromospheric signals to be affected by energetic events such as solar flares, however the link between flare activity and these oscillations remains unclear. In this work, we present evidence of changes to the oscillatory structure of the chromosphere over a sunspot which occurs during the impulsive phase of an M1 flare. Using imaging data from the CRISP instrument across the Hα and Ca II 8542 Å spectral lines, we employed a method of fitting models to power spectra to produce maps of where there is evidence of oscillatory signals above a red-noise background. Comparing results taken before and after the impulsive phase of the flare, we found that the oscillatory signals taken after the start of the flare differ in two ways: the locations of oscillatory signals had changed and the typical periods of the oscillations had tended to increase (in some cases increasing from $<$100 s to $\sim$200 s). Both of these results can be explained by a restructuring of the magnetic field in the chromosphere during the flare activity, which is backed up by images of coronal loops showing clear changes to magnetic connectivity. These results represent one of the many ways that active regions can be affected by solar flares.

Key words: Sun: chromosphere – Sun: flares – Sun: oscillations.

1 INTRODUCTION

Much of the variation we see in our observations of the Sun is essentially random in nature, and is described as noise. However, there are many sources of true periodic signals which can be identified, such as the 11-yr sunspot cycle, the p modes seen at the photosphere, and the 3-min chromospheric oscillations. These periodicities are well established and are always present in the Sun, but there are also many transient phenomena which produce oscillatory signals. Examples include coronal loop oscillations (Aschwanden et al. 1999; Nakariakov & Verwichte 2005) and quasi-periodic pulsations (QPPs) seen during solar flare activity, which have been observed across the electromagnetic spectrum and at time-scales ranging from sub-second to hours (Van Doorsselaere, Kupriyanova & Yuan 2016).

The 3-min chromospheric observations were first reported in the 1970s (Bhatnagar & Tanaka 1972) and their origin is thought to be linked to the photospheric p modes, driven by activity in the solar interior. Different explanations have been suggested and modelled in the past, such as a resonant chromospheric cavity (Leibacher & Stein 1981), but the prevailing theory is that the 3-min signature is an intrinsic property of the chromosphere caused by its acoustic cut-off frequency (Fleck & Schmitz 1991). The cut-off frequency in an isothermal atmosphere is given by

$$\omega_{\rm c} = \frac{\gamma g}{2c_{\rm S}} = \sqrt{\frac{\gamma \mu g^2}{4RT}}, \tag{1}$$

where γ is the adiabatic index, μ is the mean molecular mass, g is the gravitational acceleration, R is the gas constant, and T is the temperature. This property puts a lower limit on the frequency of acoustic (pressure) waves which can propagate through a medium, filtering out disturbances at $\omega < \omega_{\rm c}$ from the photosphere below (Lamb 1909). Using typical values for the chromosphere yields $\omega_{\rm c} \approx 0.03$ rad s^{-1}, equivalent to a period of approximately 200 s.

However, in the magnetized solar atmosphere it is necessary to think beyond the acoustic modes. In regions of high magnetic field, photospheric disturbances can convert into magnetoacoustic waves in regions where the Alfvén speed and sound speed are similar, and the resulting waves travel along magnetic field lines. Due to the Sun's gravitational field, the waves become magnetoacoustic gravity waves (MAG waves: Bel & Leroy 1977) and the cut-off frequency depends on the angle between the magnetic and gravitational fields. This leads to strong 3-min signatures above sunspot umbrae in the chromosphere, and also to running penumbral waves (RPWs: Jess et al. 2013) – where the period of oscillatory signals increases as one moves radially out from the centre of a sunspot, as the magnetic field inclination to vertical increases (Reznikova et al. 2012; Sych, Zhugzhda & Yan 2020).

There have been studies which suggest that activity from higher up in the atmosphere can affect the ubiquitous 3-min oscillations, for example plasma downflows (Kwak et al. 2016) and solar flares (Kosovichev & Sekii 2007; Milligan et al. 2017) exciting the chromosphere, and causing enhanced signals at the resonant period. Extremely powerful flares can cause sunquakes, a chromospheric signature of which has recently been observed by Quinn et al. (2019).

★ E-mail: d.millar.2@research.gla.ac.uk

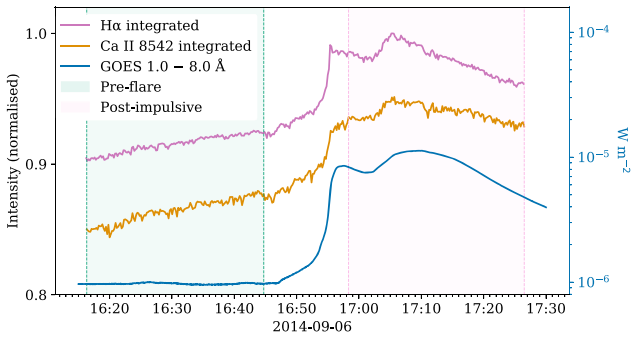

Figure 1. Light curves of GOES 1–8 Å and the H α and Ca II 8542 spectral lines from CRISP integrated across the field of view. The shaded areas indicate the two ∼30 min periods which are analysed separately: 'pre-flare' (green) and 'post-impulsive' (pink).

Specifically, oscillations over sunspots in flaring regions have been observed in the past (Kosovichev & Sekii 2007; Sych et al. 2009), but as of now the link between flare activity and sunspot oscillations is unclear.

In this paper, we study the effect of flare activity on the oscillatory signals present in an active region above a sunspot, focusing particularly on the umbra/penumbra and flare footpoints, with imaging spectroscopy data from the CRISP instrument at the SST. We aimed to identify oscillatory signals present both before and after the onset of the flare, to observe if the flare activity had induced oscillatory behaviour, or affected the signals which were present beforehand.

In Section 2, we overview the flare, describe the data sets used and the initial processing steps; in Section 3, we outline the methods used to identify oscillatory signals in the data; Section 4 outlines the main results from our analysis; we discuss limitations to our methods and possible interpretations of the results in Section 5 before concluding in Section 6.

2 EVENT AND DATA SETS

The M1.1 flare SOL2014-09-06T17:09 occurred in active region AR 12157 (−732", −302"). The analysis presented below is based on data from the CRisp Imaging SpectroPolarimeter (CRISP: Scharmer et al. 2008) instrument at the Swedish Solar Telescope (SST: Scharmer et al. 2003), and the Atmospheric Imaging Assembly (AIA: Lemen et al. 2012) on the Solar Dynamics Observatory (SDO: Pesnell, Thompson & Chamberlin 2012). The flare timeline is shown in Fig. 1 with light curves from GOES 1–8 Å and also from the CRISP instrument. Context images of the region during the flare activity from CRISP and SDO are shown in Fig. 2, and the image coordinates used in the figures throughout this paper are displayed in relation to these images.

Individual pixels in the CRISP data show an extremely rapid increase in brightness during the flare onset at approximately 16:56 (see Fig. 1), and the AIA channels contain many saturated pixels at this time. These two effects are detrimental to the analysis of oscillatory signals, and so two ∼30 min periods were analysed, before the flare onset (16:15–16:45, 'pre-flare') and after the initial brightening (16:57–17:27, 'post-impulsive').

2.1 CRISP

The active region was observed by the CRISP instrument on the SST between approximately 15:30 and 17:30 in H α (6563 Å) and Ca II 8542 Å, sampling the chromosphere and upper photosphere at 0.057 arcsec per pixel. The spectral dimension in H α covers ±1.4 Å with a step size of 0.2 Å and Ca II 8542 covers ±1.2 Å with step size 0.1 Å. Full spectral scans were obtained approximately every 11.6 s. The data are available on the F-CHROMA flare database (f-chroma.org).

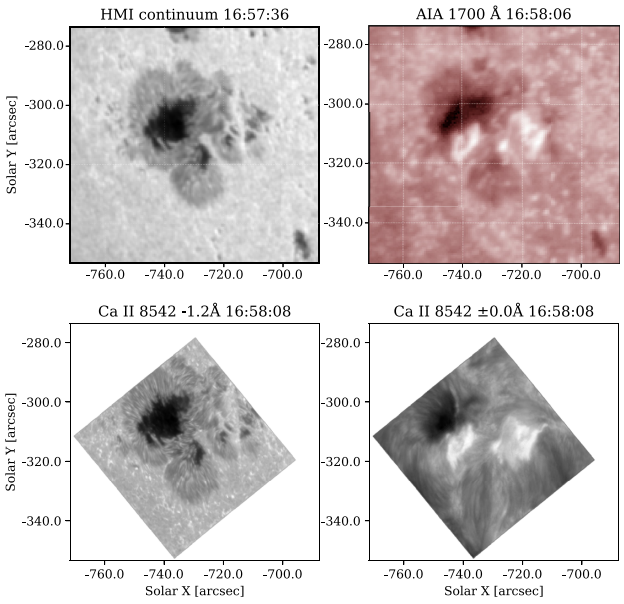

Figure 2. The area observed by CRISP at a time just after the flare onset, in several wavelengths from CRISP and SDO. The line wing (lower left) displays the photosphere, similar to the HMI/SDO continuum image (upper left), while the line core (lower right) shows the chromosphere and can be compared to the AIA/SDO 1700 Å image (upper right).

The CRISP images are aligned such that solar North points upwards along the y-axis, and the field of view rotates and moves, keeping features of interest fixed at the same pixels throughout the observation. For each 30 min analysis window (pre-flare and post-impulsive), only pixels which were in the field of view for the whole window were analysed. This accounts for the odd shape of the analysed field which will be seen in future figures.

The images were originally of dimension (1398, 1473), but were re-binned by a factor of 10 to be dimension (139, 147), after clipping the edges of the images. Time series for analysis will be drawn from each 10 × 10 macropixel. This was done to reduce the effects of seeing, and to reduce the required computation time.

2.2 AIA

The AIA on NASA's SDO provides full disc images of the Sun in eight EUV channels with a cadence of 12 s, and two UV channels with a cadence of 24 s, all at a resolution of 0.6 arcsec per pixel. The various channels observe a range of temperatures in the solar atmosphere, roughly corresponding to different heights, from photosphere to corona. The channels used in this analysis were 1600 and 1700 Å. Other AIA channels were not used, as they were greatly affected by the brightness increase caused by the flare activity, with much saturation and blooming continuing well after the flare peak, mostly in bright loop structures.

AIA images for the chosen channels were obtained and prepped using the SUNPY package (Mumford et al. 2020), before cutting out an area of interest slightly larger than the CRISP field of view with the SUBMAP method, and accounting for so-

lar rotation with the `MAPSEQUENCE_SOLAR_DEROTATE` function from `SUNPY.PHYSICS.SOLAR_ROTATION`.

3 SPECTRAL ANALYSIS

To identify and characterize periodic signals in the data, we calculated the power spectral density (PSD) of each macropixel's time series. The PSDs were then fitted with different models which describe different shapes of power spectra we expected to observe. This method was first used to identify QPPs in flare data by Inglis, Ireland & Dominique (2015), and the methods described next are adapted from this work as well as studies by Auchère et al. (2016) and Battams, Gallagher & Weigel (2019).

The power-law nature of the background noise means that identifying true oscillatory signals is not as easy as identifying the frequency bin in the power spectrum with the highest value of power. Methods exist to filter out long period signals in the time series in order to identify interesting signals; examples include analysing the time-derivative of the data (Simões, Hudson & Fletcher 2015), Fourier filtering (Milligan et al. 2017), and box-car smoothing (Dolla et al. 2012). The advantage of the spectral fitting method used here is that the original data are altered as little as possible.

3.1 Obtaining PSD

The PSD of a time series gives the 'power' of periodic signals as a function of frequency. First, each time series from individual macropixels was normalized by subtracting its mean and dividing by its standard deviation. The next step was to apodize the time series (multiplying by a Hann window function). The window function reduces spectral noise by removing the discontinuity between the first and last entry in the time series. The PSD was then obtained by performing a fast Fourier transform, and taking the absolute value of the result.

3.2 Spectrum models

When the PSD is plotted in log-space, the shape of the spectrum can be identified. A flat line corresponds to perfect 'white' noise, whereas a sloped line represents 'red' noise. Formally, the colour of noise is determined by the α parameter in the following equation, which gives the power, P, as a function of frequency, f:

$$P(f) = Af^{-\alpha}. \tag{2}$$

A is a constant which affects the vertical offset of the sloped line.

In a signal originating from purely coloured noise with a single spectral index, the spectrum would be described well by equation (2). However, in reality the time series we observe can be better described by an altered version of this simple power law. In this work, we examine three different models to describe the observed PSDs.

The first model (M1: equation 3) which is used for the spectra is a power law with an additional constant, C, to describe a white-noise element in the data from photon counting (technically this is two power laws summed together, one of which has index $\alpha = 0$):

$$\mathrm{M1} = Af^{-\alpha} + C. \tag{3}$$

In Fig. 3, a spectrum is shown which is best fit by the power-law noise model (M1) and shows the types of random variations which can be attributed to coloured noise. The second model (M2: equation 4) includes a Gaussian bump term – utilized also by Inglis et al. (2015) – which is used to indicate enhanced oscillatory power in addition to the power described by M1. An additional three

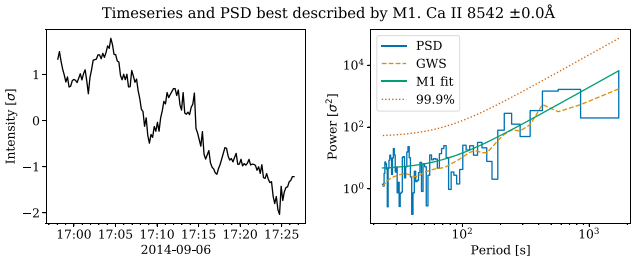

Figure 3. The time series (left-hand panel) and corresponding PSD (right-hand panel) taken from a macropixel from the line core of Ca II 8542 at a location far from the main sunspot and the flare activity. Plotted with the PSD (blue stepped line) is the global wavelet spectrum (yellow dashed line), the mean spectrum fit by M1 (green line), and the 99.9 per cent significance level (orange dotted line, explained in Section 3.3).

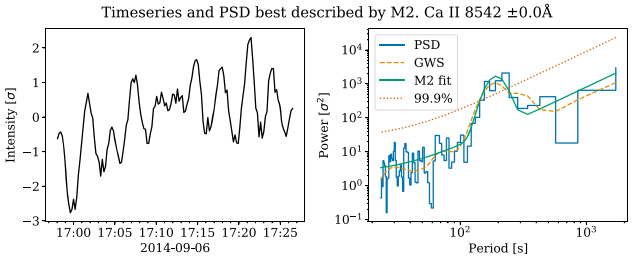

Figure 4. As in Fig. 3, but showing results from a macropixel over the sunspot umbra. The confidence threshold (orange dotted line) is shown corresponding to the noise background if there was no bump present. The peak of the Gaussian bump occurs at $\beta = -5.26$ which corresponds to a period of ≈ 190 s.

parameters are introduced to describe the height (B_G), width (σ), and position of the peak in frequency space (β):

$$\mathrm{M2} = \mathrm{M1} + B_\mathrm{G} \exp\left(\frac{-(\ln \boldsymbol{f} - \beta)^2}{2\sigma^2}\right). \tag{4}$$

An example of an M2 spectrum is displayed in Fig. 4. The spectrum shown in this figure is clearly of a different nature to its Fig. 3 counterpart, and it is well described by a bump rising above a coloured-noise background. The time series has a clearly visible oscillatory signal which produces a PSD with a clear increase of power around the approximate period of the oscillations. The oscillations are not all of exactly equal length, and so the signal in the PSD is spread out somewhat, producing the bump. The parameter β gives us an idea of the most common periodicities observed in the time series, and can be converted to a period via $T = \mathrm{e}^{-\beta}$.

When observing some of the PSD fits using M1 and M2, it was found that often the PSD would appear to level off below certain frequencies, and this behaviour could not be described accurately by M1 or M2. We introduce a third model (M3: equation 5) which utilizes a kappa function, and has been used in the past by Auchère et al. (2016) and Threlfall, De Moortel & Conlon (2017):

$$\mathrm{M3} = \mathrm{M1} + B_K \left(1 + \frac{f^2}{\kappa\rho^2}\right)^{-\frac{\kappa+1}{2}}. \tag{5}$$

In the above equation, ρ describes the width of the kappa function, κ describes its extent into the high-frequency wing, and B_K gives its height. See Fig. 5 for an example of a spectrum which was fitted by M3. It is clear from the time series that there is oscillatory behaviour here, however it is not sufficiently well localized to any particular frequency to create a defined bump. While it is possible that the

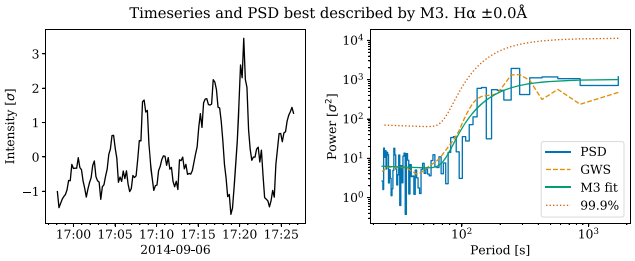

Figure 5. Similar to Figs 3 and 4, but for a macropixel from the core of H α over the sunspot penumbra, which has been best fit by the kappa function (M3).

kappa function gives some information about oscillatory behaviour, it is more complex to define than the Gaussian bump case. In Fig. 5, the oscillations are drifting in period over the ∼30 min window, which could create a wide increase in power which manifests in the kappa-shaped bulge. An apparent flattening of the spectrum could be caused by enhanced power at shorter periods or a decrease in power at longer periods.

While there have been theories put forward as to why a power-law noise spectrum describes a solar time series – for example due to many small energy deposition events (Aschwanden 2011), there is little explanation for why a PSD should take the shape of a Gaussian bump or kappa function, as opposed to any other shape. Battams et al. (2019) used a Lorentzian bump instead of Gaussian, motivated by its physical meaning in the context of a damped oscillator. However, we found more success fitting the PSDs from this data set when using the Gaussian option. In this context, these models can be seen as tools to identify PSDs which deviate from simple coloured noise, rather than descriptors of the physical processes behind the observed time series and PSDs.

The fitting process was performed in Python using the `CURVE_FIT` function from the `SCIPY` library (Virtanen et al. 2020). The individual data points for the power spectra span many orders of magnitude, so the squared residuals must be weighted to be comparable. Following Auchère et al. (2016), the global wavelet spectrum (GWS) was used as a weighting function. The GWS is a proxy for the PSD of the time series, and is calculated by time-averaging the wavelet transform, as described by Torrence & Compo (1998). It is assigned to the 'sigma' argument in `CURVE_FIT`.

3.3 Identification of significant oscillatory signals

Identifying true oscillatory signals above noise is a very difficult task without visually inspecting each time series and spectrum, and therefore we set a number of criteria that each spectral fit must first meet. The first criterion to identify an M2 fit is that the Gaussian bump model must describe the observed data better than M1 and M3, based on a weighted residuals squared (WRS) measurement of each fit (weighted using the GWS). M2 and M3 have three more free parameters than M1, and so these would be expected to fit better in most circumstances. An F-test is used when comparing models with different numbers of parameters, with the F-statistic defined as

$$F = \frac{\left(\frac{WRS_1 - WRS_2}{k_2 - k_1}\right)}{\left(\frac{WRS_2}{N - k_2}\right)}. \quad (6)$$

In this equation, k is the number of parameters for each model and N is the number of data points in the PSD. The null hypothesis for the F-test is that M1 describes the data as well or better than M2 (or M3) and a p-value to reject it is obtained based on the value of F in the $F(p_2 - p_1, n - p_2)$ distribution. This p-value threshold is $p < 0.001$ for the majority of the analysis. It should be noted that a p-value below the threshold does not indicate that M2 (or M3) describes the data perfectly (or well at all), just that it is preferred over M1, and the test is expected to be wrong 0.1 per cent of the time.

A 99.9 per cent confidence level may seem rather stringent, however reducing the confidence level will introduce false positives; we believe that avoiding this is important. The same analysis done using a 95 per cent level returned more M2 results, and the overall occurrence patterns and changes were the same as those obtained using the 99.9 per cent confidence level. But on inspection of individual power spectra and their fits, many M3-like spectra, with a kappa function appearance, had been incorrectly assigned as M2 at the 95 per cent confidence level. Since the main results remained the same, the 99.9 per cent was preferred in this case.

Spectra which are best described by M2 and which pass this F-test were then identified to have two main components: a Gaussian bump and a background noise spectrum described by M1. The background spectrum is found by using the parameters from the M2 fit, but setting the B_G parameter to zero, removing the bump. The significance of the bump was tested against the background noise level, based on a confidence threshold obtained using the parameter m from the following equation:

$$m = -\ln(1 - X^{1/N}). \quad (7)$$

This equation states that each of the N frequency bins of the PSD has a probability X of being m times greater than the background noise spectrum. It is obtained from the fact that the Fourier spectrum is χ^2_2 distributed around the mean power value at each frequency, and is explained fully in Auchère et al. (2016). The spectral bump is taken to be significant if the fitted spectrum is more than m times the background spectrum at a confidence level of 99.9 per cent. By applying these two different significance tests to the data the likelihood of identifying a time series which does not contain a significant deviation from the standard background noise was greatly reduced.

The final step in determining the significance of each Gaussian bump was to remove results which contained bumps very close to the edges of the spectra. Results were only kept which satisfied $-6.1 < \beta < -3.91$, these limits corresponding to approximately 450 and 50 s periods, respectively. This range was necessary because of the limitations of the data, that is, the cadence of 12 s setting a lower limit to the detectable periods and the total length of each time series of approximately 30 min setting an upper limit.

4 RESULTS

4.1 Preferred models

The methods described in Section 3 allowed a preferred model (M1, M2, or M3) to be assigned to each macropixel in our pre-flare and post-impulsive data, at several wavelength points across the H α and Ca II 8542 Å spectral lines. Visualizations are found in Figs 6–9, and display the areas of oscillatory signals at these different wavelength points, overplotted with contours showing the outlines of the sunspot umbra and penumbra and coloured patches showing the positions of the flare footpoints.

The first thing to note from these plots is that M1, the power-law coloured-noise model was the most common result, being the preferred result in 83 per cent of all pixels, compared with 6 per cent

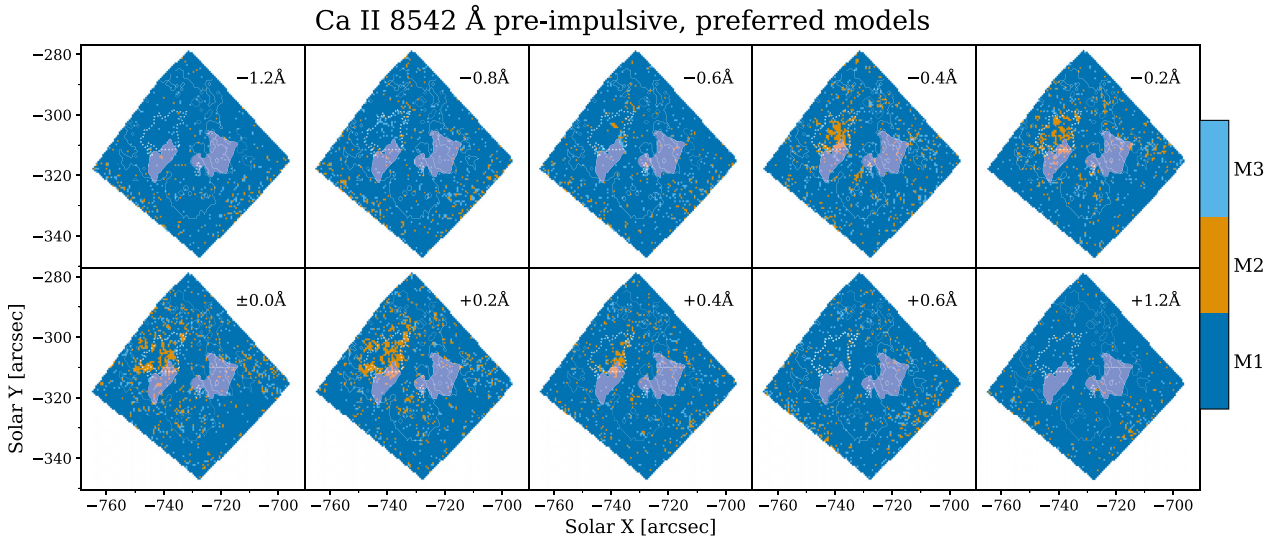

Figure 6. The models which best describe the spectra of individual macropixels at several points across the Ca II 8542 Å line, during the pre-flare period (16:15–16:45). Each model is assigned a different colour, and the edges of the sunspot umbra and penumbra (drawn from 40 per cent and 75 per cent intensity levels of the first wing image) are shown in dotted and solid contours, respectively. The locations of the flare footpoints are indicated by the semitransparent solid patches, showing pixels over 55 per cent of the maximum intensity of a line core image from the post-impulsive period.

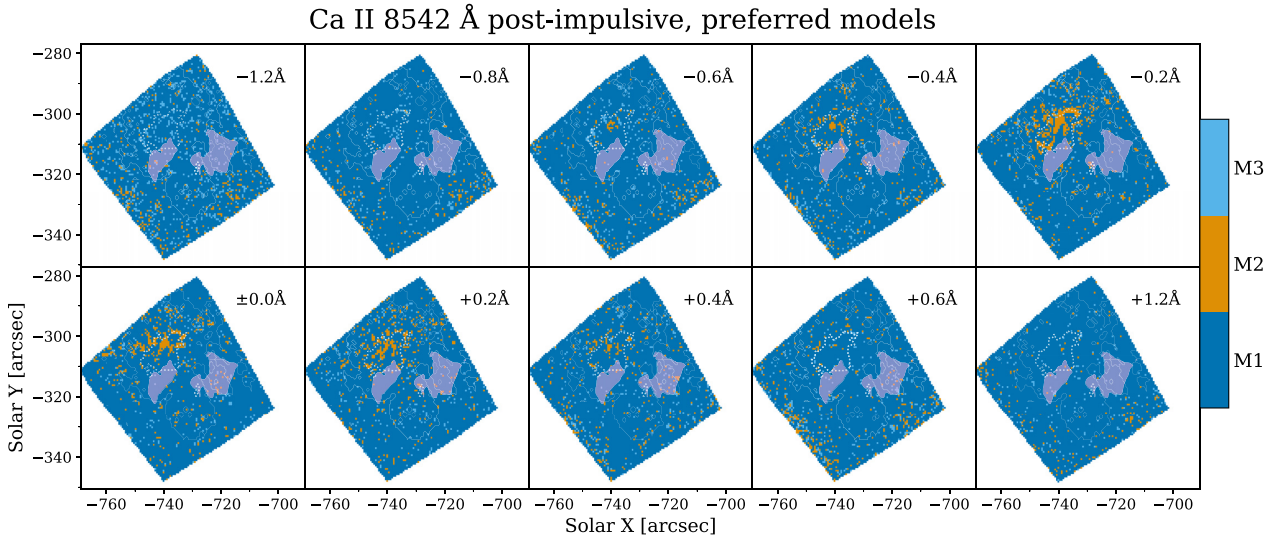

Figure 7. Similar to Fig. 6 but during the post-impulsive period (16:57–17:27). The shape of the plots is different than in the pre-flare case because of the rotation of the CRISP field of view. Note the northern umbra–penumbra border with concentrations of M2 fits at several wavelengths.

for M2 which includes the Gaussian bump, and 11 per cent for the M3 kappa function. This is unsurprising as M1 is the simplest and therefore most generally applicable shape of the three. Table 1 shows the percentage of M2 and M3 fits which were assigned to macropixels in select wavelengths and in both the pre-flare and post-impulsive time periods.

Broadly, it appears that more M2 fits are found for power spectra at wavelengths closer to the centres of the lines, out to ±0.4 Å, and areas with many M2 fits are found over the sunspot umbra, and around its border. As we move in wavelength away from the line core towards the wings, the occurrence of M2 fits drops considerably. Many more pixels in the wings show fits to M3, especially in the post-impulsive data for both lines.

Although there appears to be correlation between the positions of M2 fits and the sunspot umbra, there is not much distinction between the penumbra of the sunspot and the surrounding area.

The locations of the oscillatory signals compared to the flare footpoints are another important aspect to the results. These locations are superimposed on both the pre-flare and post-impulsive results (Figs 6–9), for easy reference between figures. There appears to be little to no oscillatory behaviour at the locations of the flare footpoints in the post-impulsive results, with most of the M2 fits located near the northern umbra–penumbra border. There were however some signals of oscillations at the location of the eastern ribbon in the pre-flare data, which may indicate the effect of the flare on the oscillations. This is discussed in more detail in Section 5.2.

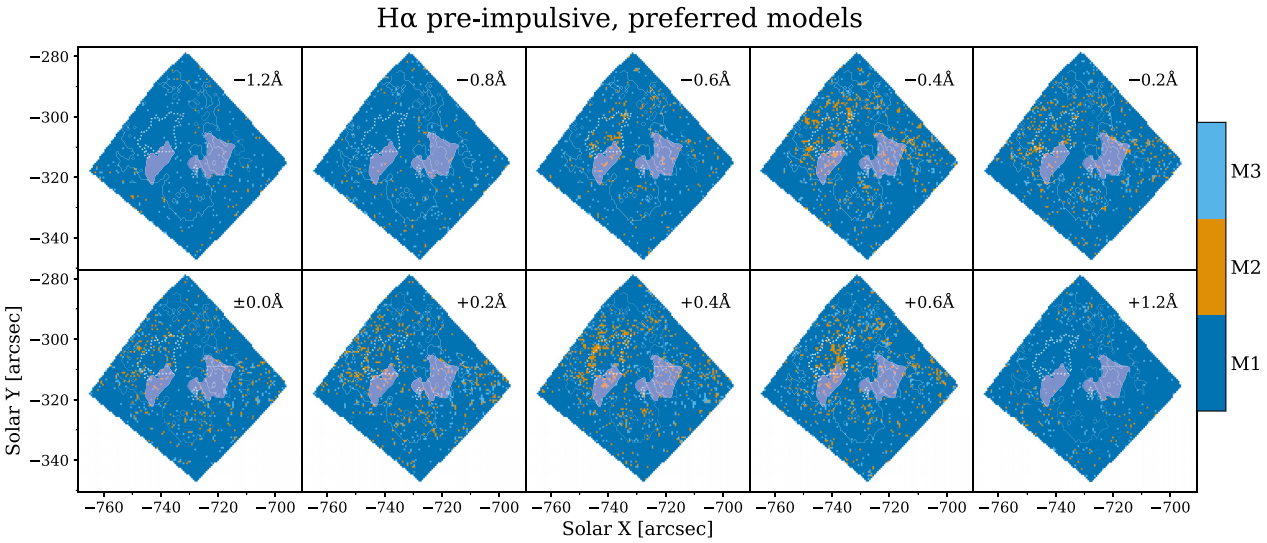

Figure 8. Similar to Fig. 6 but for the H α line.

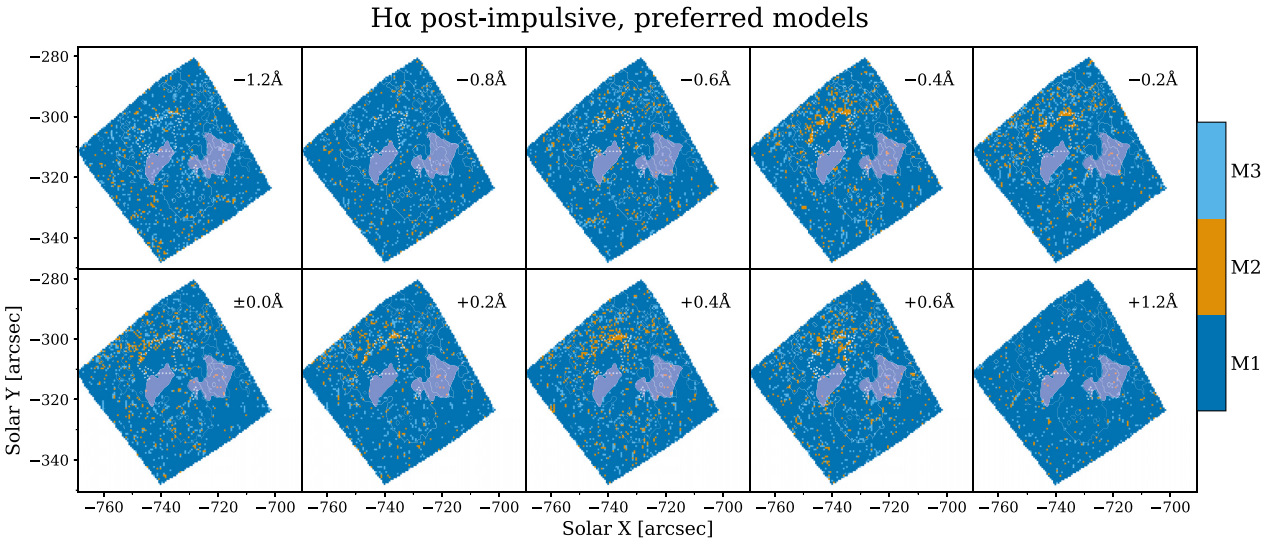

Figure 9. Similar to Fig. 6 but for H α, after the initial flare activity.

4.1.1 Calcium 8542 Å preferred models

Before the flare onset in the 8542 Å line, M2 fits are found concentrated over the sunspot umbra at the line core, with the results at ± 0.2 Å looking similar (Fig. 6). Moving away from the core, at the ±0.4 Å positions there are some M2 fits over the umbra but these are much more concentrated spatially. Further from the core, M2 fits are very scarce, with the majority of the pixels being described best by the standard coloured-noise background (M1).

After the impulsive phase of the flare, the appearance of the 8542 Å results is quite different (Fig. 7). There is an increased number of M3 fits, in particular in the line wings, and a decreased number of M2 fits in general. The −0.2 Å position seems to show an enhancement of M2 fits over the umbra, while at the line core and at the +0.2 Å position the number of M2 fits has dropped, and there is a change in the location of the oscillatory signals – the positions where M2 fits occur is in fact quite different from the pre-flare case. The places showing M2 fits in the line core and +0.2 Å positions during the post-impulsive period are now mostly at the northern umbra–penumbra border, rather than more towards the centre of the sunspot (compare with Fig. 6).

4.1.2 H α preferred models

The results for H α are in some ways very similar to the Ca II 8542 Å case. For example, there are more M3 fits towards the far wings and in the post-impulsive data, however, unlike Ca II 8542 Å the M2 model fits are most prevalent in the +0.4 Å and +0.6 Å line positions, as opposed to the line core. Also, the area where M2 was the preferred fit is far smaller in both the pre-flare and post-impulsive cases than their counterparts in Ca II 8542 Å. Unlike for Ca II 8542 Å, there seems to

Table 1. Percentage of all macropixels which had preferred model fits M2 (Gaussian bump) and M3 (kappa function) for each wavelength and for the pre-flare and post-impulsive periods.

Wavelength	Pre M2 (per cent)	Pre M3 (per cent)	Post M2 (per cent)	Post M3 (per cent)
8542 − 1.2 Å	1.9	2.9	3.9	9.5
8542 − 0.8 Å	3.1	4.8	2.5	4.0
8542 − 0.6 Å	2.7	3.9	3.2	4.6
8542 − 0.4 Å	5.7	4.9	4.2	4.0
8542 − 0.2 Å	5.7	3.8	7.1	3.3
8542 ± 0.0 Å	7.1	4.7	5.6	2.7
8542 + 0.2 Å	7.8	4.1	5.7	3.1
8542 + 0.4 Å	4.1	3.6	4.2	3.8
8542 + 0.6 Å	3.2	4.4	4.4	4.6
8542 + 1.2 Å	1.6	1.9	2.2	2.5
Hα − 1.2 Å	0.7	1.7	3.2	8.1
Hα − 0.8 Å	0.9	2.5	2.2	5.9
Hα − 0.6 Å	2.7	2.3	3.6	6.5
Hα − 0.4 Å	5.9	3.6	5.1	6.7
Hα − 0.2 Å	4.6	3.8	4.8	7.7
Hα ± 0.0 Å	3.4	3.3	4.4	6.6
Hα + 0.2 Å	4.9	4.3	3.8	5.6
Hα + 0.4 Å	6.3	4.0	5.6	6.8
Hα + 0.6 Å	5.3	4.2	4.5	7.3
Hα + 1.2 Å	1.0	2.8	1.5	3.2

be very little evidence of concentrated oscillatory signals before the flare occurs, even at the centre of the sunspot, except in the +0.4 Å and +0.6 Å panels of Fig. 8.

After the impulsive phase, Hα shows a large number of M3 fits which are not only confined to the wings of the line. Unlike the Ca II 8542 Å line, in many wavelength positions it appears that after the impulsive phase there has been an increase in the number of macropixels showing oscillatory signals, and we see lots of M2 fits occurring from the core out to ± 0.6 Å. While the total area of M2 fits is fairly sparse compared to 8542 Å, there is a considerable amount of oscillatory signal focused on the northern umbra–penumbra border where there was a lot less in the pre-flare results.

4.2 Periods and locations of Gaussian bump peaks

In pixels where M2 was the preferred fit, we can use the periods at which the Gaussian bumps in M2 peak to diagnose the characteristics of the oscillatory signals coming from those pixels. These results are shown in Figs 10–13 for the Ca II 8542 Å and Hα lines, in both the pre-flare and post-impulsive time periods.

From these plots we see a difference in the periods of the bump peaks when moving from the centre of the sunspot outwards. In general the periods of the oscillatory signals are shorter in the centre of the sunspot, at 100–150 s, and gradually increase into the 200–250 s range towards the edges of the umbra. In the penumbra the periods reach 300 s and above. This is most clearly seen in the Ca II 8542 Å data, but the effect is present in both lines.

These results could be interpreted similarly to those of Reznikova et al. (2012) and Jess et al. (2013), as evidence of a changing magnetic field inclination from the centre of the sunspot outwards.

There are some differences between pre-flare and post-impulsive results, with periods in post-impulsive data tending to be longer than in the pre-flare case. Again this is clearer to see in Ca 8542 Å results (compare the ±0.2 Å and line core panels of Figs 10 and 11), mostly due to the larger area of M2 pixels in this line, compared to Hα. This again could be caused by a differing magnetic field inclination. However, in this case the difference between pre-flare and post-impulsive period distributions could suggest that the magnetic field through the sunspot chromosphere has been affected by the flare itself, perhaps because of the reconfiguration of magnetic field taking place during the flare.

4.3 AIA results

The preferred models found for pixels from AIA 1600 and 1700 Å are shown in Fig. 14, containing both pre-flare and post-impulsive results. These plots are in contrast to those in Figs 6–9 in that there is little convincing evidence whatsoever of concentrated oscillatory signals above the sunspot, or in the active region. Instead, there is an abundance of M2 fits seen outside the active region, around the edges of the plots. These match spatially with the intensity of the ultraviolet channels: immediately surrounding the sunspot umbra and penumbra is a large region of brighter plage, where scarce oscillatory signals are seen.

Table 2 shows the percentage of M2 and M3 fits for the AIA channels. This table and also Fig. 14 show that the 1700 Å channel has far more pixels containing oscillatory signals than the 1600 Å filter. There is also little change in the number of M2 fits between the pre-flare and post-impulsive periods in either channel.

The most noticeable change between the pre-flare and post-impulsive results is the appearance in post-impulsive data of many pixels best fitted by M3, at locations near the flare ribbons. As discussed in Section 3.2, a successful fit to M3 does not directly tell us anything about oscillatory behaviour, however we can say that these time series must have deviated significantly from the coloured-noise background, which is perhaps to be expected due to the large variations in brightness in these pixels.

5 DISCUSSION

5.1 Limitations

In this study, we have analysed intensity variations at specific wavelengths, however there are several physical effects which can contribute to the fluctuations in brightness at a particular wavelength, including Doppler shifts of the core of the line. Other approaches to the detection of oscillations utilize such velocity signals, particularly in the photosphere where intensity variations are hard to detect (Khomenko & Collados 2015). While using the evolution of the line profiles to infer velocity oscillations in our observations would allow a more in-depth understanding of the physical reasons for the oscillation, in terms of what we focus on here – the locations of the oscillations and their changes – we expect that this would return similar results to our investigation based on intensity. In fact, upon inspection of the evolution of spectral line shapes in these data, while macropixels with strong velocity signals also produced an oscillatory behaviour in intensity at a particular wavelength, as would be expected, we also found that intensity oscillations were not always accompanied by clear changes in the spectral line shape. Such cases could have been missed by an analysis relying on line shifts. In this respect our approach is just as valid as one based on spectral line profiles, while being simpler to carry out. Nevertheless, care should be taken when drawing conclusions from these results, and there is certainly more to be learned from the full line profiles.

While the spectral fitting method used here is a powerful technique and has been proven useful in many previous studies, there are limitations to its effectiveness.

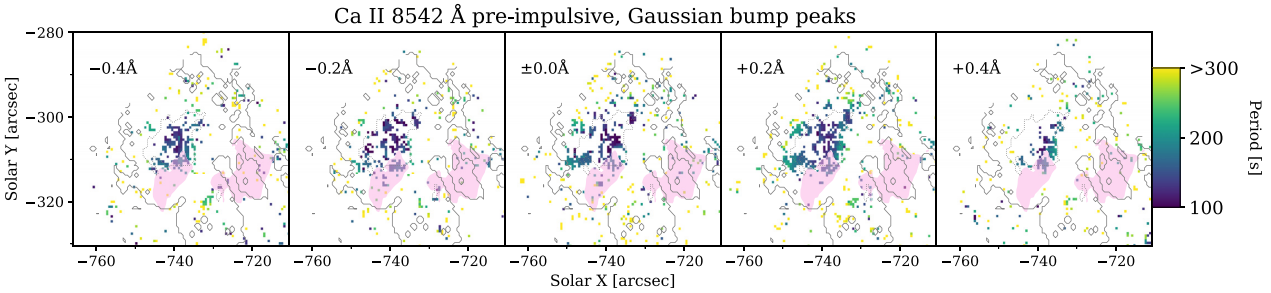

Figure 10. This plot is similar in layout to Fig. 6 but it shows periods at the peaks of Gaussian bumps, in macropixels where M2 was the preferred fit. Those macropixels which were not best fitted by M2 are left blank. This shows the difference in the period of oscillatory signals which are seen at different spatial positions across the images. In general, the period of the oscillations is shorter towards the centre of the sunspot. The contours showing the umbra and penumbra are identical to Figs 6–9, and the footpoints are shown similarly.

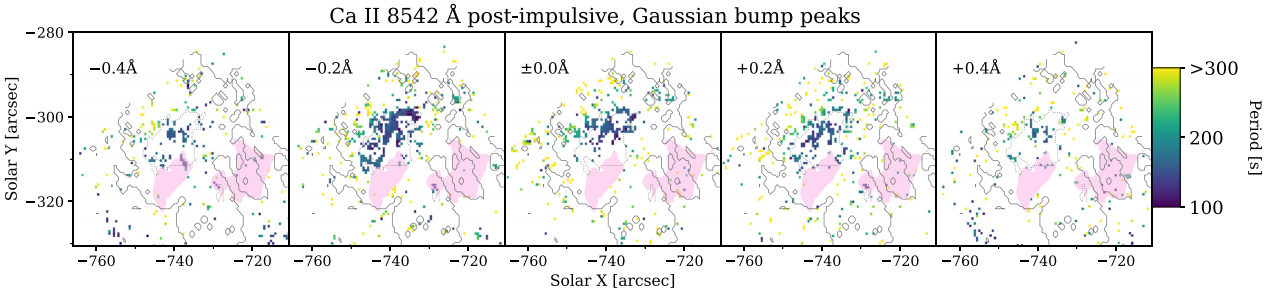

Figure 11. Similar to Fig. 10 but for the post-impulsive period.

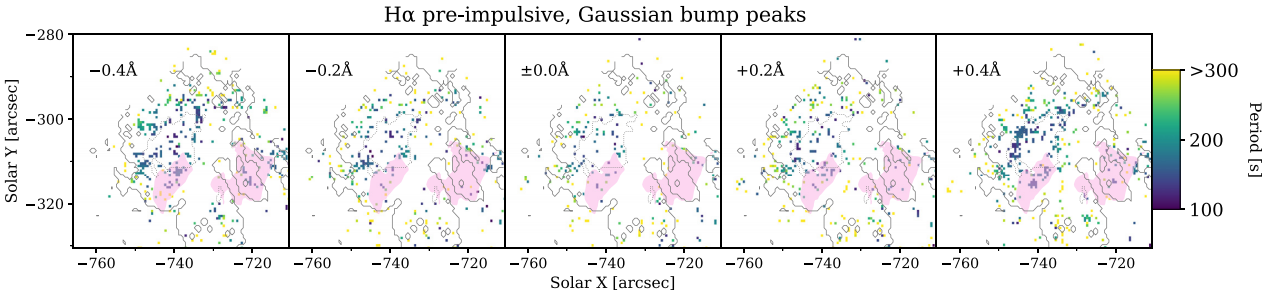

Figure 12. Similar to Fig. 10 but for the Hα line.

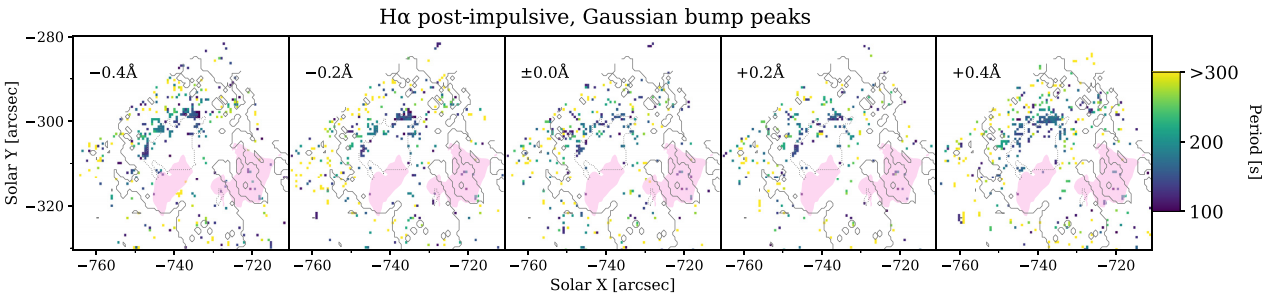

Figure 13. Similar to Fig. 10 but for Hα in the post-impulsive period.

One of the first things to consider is our choice of models. The results of this methodology are dictated by the models, as the data are forced to fit one of three models we choose. For example, if some process exists which produces two separate periods in the same time series, the resulting PSD could contain two bumps. This could either cause the curve fit algorithm to select one of these two bumps and not the other, or it could fail to fit the single bump model altogether. The case of double periods has been known to

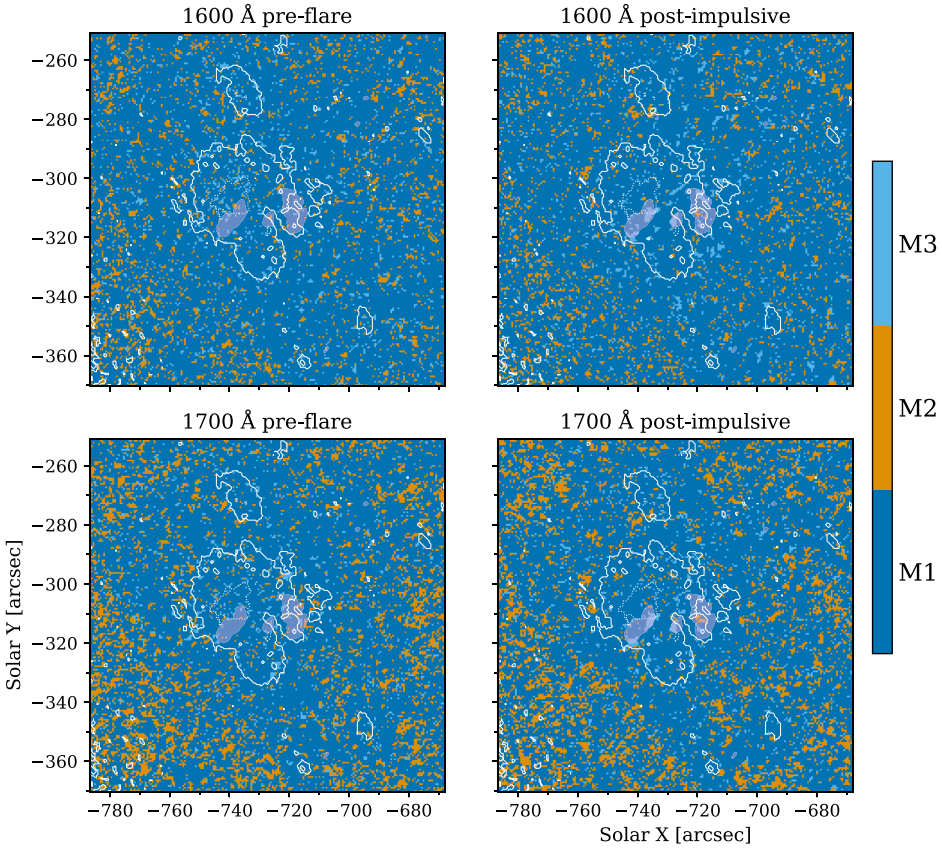

Figure 14. Similar to the corresponding plots for CRISP wavelengths (Figs 6–9) but for the two AIA channels, with pre-flare and post-impulsive displayed on the left and right, respectively. Note the field of view is slightly larger than in the CRISP figures. Overplotted are contours of 30 per cent and 73 per cent intensity from the first HMI continuum image to show the positions of the sunspot umbra and penumbra. The filled contours at over 15 per cent of the maximum intensity in 1700 Å at the beginning of the post-impulsive period show the locations of the flare footpoints.

Table 2. The percentage of all pixels in AIA wavelengths which had preferred fits M2 and M3, for the pre-flare and post-impulsive time periods.

Wavelength	Pre M2 (per cent)	Pre M3 (per cent)	Post M2 (per cent)	Post M3 (per cent)
AIA 1600 Å	9.2	4.9	8.6	5.7
AIA 1700 Å	15.8	4.4	15.9	5.1

happen in QPP data (Inglis & Nakariakov 2009), and could be better handled by e.g. wavelet analysis. However, wavelet analysis is difficult to automate for large data sets like the one studied here.

One of the main reasons the kappa-shaped model was fitted in addition to the coloured-noise background and Gaussian bump models was due to the initial choice of models being insufficient. On inspection of M2 fit results by eye, some spectra were selected as an M2 fit when they had flattened off in the low-frequency regime, instead of returning to the red-noise background level. These poor results at the low-frequency part of the PSDs could have been because the fitting technique is biased towards the high-frequency end, due to the nature of the frequency space covered by the Fourier transform (more frequency points at high frequencies leads to a greater influence on the goodness of fit).

The CRISP observation for this data set finished at approximately 17:30, putting limits on the length of the post-impulsive time series we can analyse. The length of the time series relates to the lowest frequency which can be studied using the Fourier transform. Longer time series would also reduce noise in the spectra we obtain, and hence lead to better (or at least, faster converging) fits.

5.2 Interpretations

The CRISP results showed considerable variation across the wavelength steps of the spectral lines. This could be because different points in the lines sample different heights in the atmosphere: both Hα and Ca II 8542 Å sample the mid-chromosphere at their cores (∼1 Mm, Kuridze, Mathioudakis & Simoes 2015) and the upper photosphere at their wings. Strong, isolated oscillatory signals could be present only above a certain height, beyond the altitude at which long period signals from the photosphere have decayed (as described in Section 1).

Another effect which applies here is that radiation at a particular wavelength does not always originate from exactly the same height, as its contribution function can be spread out. If there are local pressure disturbances in the atmosphere caused by MAG waves, then sampling from a wide range of heights would lead to muddied signals, with the potential for destructive interference occurring. MAG waves could be travelling through the lower parts of the sunspot chromosphere, but not be detectable in this

kind of observation because of the broad contribution function. Conversely, if we receive light which is emitted from a more vertically compact region, it is more likely that signals will be preserved.

The results in Hα and Ca II 8542 Å look very different, which raises questions as these lines are often considered to sample similar heights in the chromosphere. We do not know the exact heights at which the emergent radiation of these lines are formed, but we can look to examples from authors who have used e.g. RADYN to simulate their contribution functions, such as Kuridze et al. (2015) who used this method to synthesize the line formation for the same CRISP flare data set as we use here. As another example, Rubio da Costa et al. (2015) simulated Hα and Ca II 8542 Å lines from an M3.0 flare at both very early times (similar to pre-flare) and late times, finding no overlap in height of the contribution functions at the line cores, with Hα core emerging from 1.6–2.2 Mm and Calcium II 8542 Å emerging from 1.3–1.5 Mm. If the spectral lines behaved similarly in our case, this could account for the discrepancies between the lines, and also the lack of strong signals in Hα, as the contribution function at the core is far more spread out than its Ca II 8542 Å counterpart.

Similar effects could also explain the results from the AIA UV channels in Section 4.3. These channels are very broad filters and the heights which they sample are perhaps not precise enough to detect localized oscillations in the active region by this method. The results for the AIA 1600 and 1700 Å channels showed a lack of oscillatory signatures over the umbra, and more in the penumbra and plage. These results are similar to those obtained by Battams et al. (2019) who used a power-spectrum fitting analysis and found spectral bumps across almost the whole disc in the 1700 Å AIA channel, except in the area immediately surrounding a sunspot. The difference between the active region and 'quiet' sun results could be due to a difference in the spectral distribution of the radiation transmitted by the filters. A study by Simões et al. (2019) showed how the temperatures sampled by these filters can be different in flare and plage data, with flare data sampling the chromosphere and plage data the photosphere, generally. It is possible that in active regions the UV filters sample heights more similar to the flare data studied by Simões et al. (2019), perhaps from higher in the atmosphere with a smaller oscillatory component.

A similar phenomenon named 'height inversion' has been observed by other authors, where 3-min signals are seen to be strong in chromospheric sunspot umbrae, but almost non-existent in the photosphere which is dominated by 5-min oscillations (Kobanov, Kolobov & Chupin 2008; Kobanov et al. 2011). While Milligan et al. (2017) did find flare-related oscillatory signatures in 1600 and 1700 Å data, these were signatures integrated over a large field of view, and the flare-related oscillatory signals were during the impulsive phase which we cannot study due to saturation.

The positions where significant oscillatory bumps were identified in CRISP data appear to have changed after the flare activity. Comparing the bottom right panel of Fig. 2 to the results in Figs 6–13, we see that one of the flare ribbons develops over the lower corner of the sunspot umbra. This could explain the lack of M2 fits in this area in the post-impulsive results. The number of macropixels with M2 fits increased at the northern boundary of the umbra in most wavelengths at ± 0.4 Å, and it is possible the same would have happened at the southern boundary but the natural oscillations, which are connected to the temperature of the plasma, may have been dramatically affected by flare heating.

If we assume the oscillatory signals we detect here are caused by MAG waves travelling from below, along the sunspot field, the results from Sections 4.1 and 4.2 may be linked to properties of the magnetic field in the chromosphere above this sunspot. For instance, the areas which produced a lot of concentrated M2 fits are different in much of the pre-flare and post-impulsive results. This could be caused by the magnetic fields having a different orientation after the flare process, causing the MAG waves travelling along the field lines to be guided to a different spatial location. As a speculative example, if we consider the chromosphere to be 2000 km thick, and observe the locations of signals to move by ∼5 arcsec, this would correspond to a magnetic field line which was originally normal to the solar surface inclining by ∼60 deg. Strong, flare-related changes in field inclination have previously been inferred from line-of-sight magnetograms (Sudol & Harvey 2005) or observed in vector magnetograms (Petrie 2019).

Further evidence for the changing magnetic field interpretation can be seen in the results of Section 4.2 where the periods at which Gaussian bumps peak changed after the flare event. In MAG waves the acoustic cut-off frequency determines the period of the oscillations:

$$\omega_c = \frac{\gamma g \cos\theta}{2c_s} \propto \frac{g\cos\theta}{\sqrt{T}} \tag{8}$$

θ is inclination angle from vertical. Following this equation, the fact that g has negligible variation, and observing that temperature change is unlikely to be a factor as the areas of M2 fits were far removed from the flare ribbons and do not show any intensity variations, the inclination angle is the only factor which could cause the change in cut-off frequency in this case. Following our example from above of a 60 deg inclination change, the cut-off frequency would be halved, and the prominent period would be doubled.

To test the theory of a changed magnetic field leading to a change in the oscillatory behaviour around the sunspot, we studied data from the HMI instrument on SDO (Schou et al. 2012). To avoid the effects of solar rotation and line-of-sight changes, we accessed `HMI.SHARP_CEA_720S` dataseries from 15:00 to 19:00. This series is a reprojection of the magnetic field into three cylindrical equal area (CEA) components: B_r, B_ϕ, and B_θ, and is available at a cadence of 12 min (Hoeksema et al. 2014). We looked for evidence of magnetic field changes at the time of the flare activity which were not part of a more gradual change of the field. We investigated the site where oscillatory behaviour was detected after the flare impulse but not before (the northern umbra–penumbra border), and found no significant evidence of field changes which correlated to the appearance of the oscillations. Conversely, there were several areas where there were oscillations before the flare which seemed to disappear after the impulsive phase. Previously we found similar behaviour under the flare footpoints and attributed the lack of oscillations in post-impulsive data to the flare heating. When analysing the HMI time series we found that there were many locations which lost oscillatory signal after the flare activity but were not under the footpoints, and instead showed sudden changes to one or more of the magnetic field components.

In Fig. 15, we show several examples of magnetic field time series at a variety of locations. Time series 1 is under the flare footpoint and shows a clear, abrupt, and persistent change to the B_θ and B_ϕ components during the flare impulse. Time series 4 shows a change to the radial component of the field B_r, and is located very near the flare footpoint, where oscillatory signal was lost after the flare. Towards the centre of the umbra, away from the footpoints are points 3, 5, and 6, whose time series show changes to B_r and show a lack of oscillations after the flare activity. While this evidence of changing magnetic field parameters could explain why the oscillations at these locations was interrupted, we also find many examples of locations

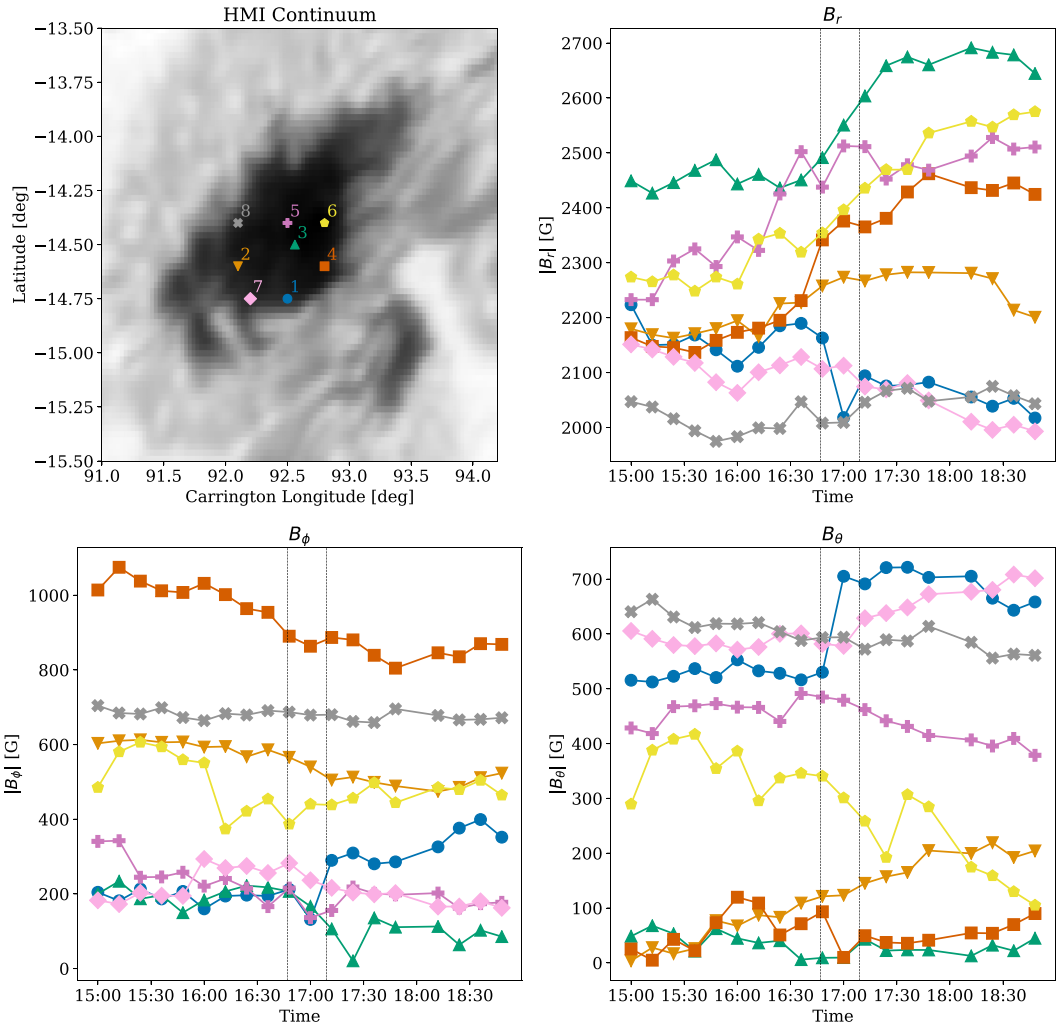

Figure 15. Time series of the three CEA magnetic field components measured by HMI, taken from selected points in the sunspot umbra. The vertical lines show the times of the start of the impulsive phase and the time of the flare peak.

where the magnetic field did not change considerably, such as at points 2, 7, and 8.

From our analysis of HMI data, there were no obvious signs of field changes which correlated with all of the changes in oscillatory behaviour we observed with CRISP, however we found evidence of strong field changes at locations where oscillations disappeared after the flare. An important distinction here is that HMI samples the photosphere, and the CRISP line cores sample the chromosphere. The chromosphere is such a magnetically complex part of the atmosphere that HMI magnetic field values do not necessarily match to e.g. measurements of the chromospheric magnetic field from chromospheric spectropolarimetry (Kleint 2017).

To investigate our interpretations further, we have plotted in Fig. 16 images from AIA's 171 Å channel, one from before the flare and one from the end of the CRISP observing window. This channel is the most suitable to get an impression of the magnetic activity in the active region. The flare ribbons seen in the CRISP line cores are linked by a newly formed hot loop, which develops after the flare activity into the bright structure shown in Fig. 16. Other larger loop structures are seen emerging from the active region, to the east and north-east of the flare footpoints and sunspot umbra. It can be seen that these loops undergo changes during the flare activity, with some contraction of the loops visible. It is clear from observing this particular wavelength that the magnetic structures in this active region have been altered during the flare activity and this gives weight to our interpretation regarding a change of the magnetic field inclination.

6 CONCLUSIONS

We studied this active region to try and understand the types of oscillatory signals which can be affected or induced by flare activity. We found significant oscillatory behaviour consistent with the theory of MAG waves both before and after the flare. In this first spectrally resolved analysis of flare chromospheric oscillations using the spectral fitting method, we found that the periodic signals seen in H α and Ca II 8542 Å line core observations were not seen in the line wings or the AIA ultraviolet channels, possibly due to the broader range of heights sampled by these observations.

There is evidence of the oscillatory behaviour being altered indirectly by the flare, both in the locations of the signals and the periods of the oscillations. The signals were found to have moved from covering almost the whole sunspot umbra before the flare, to being concentrated on the northern umbral border afterwards. There was a

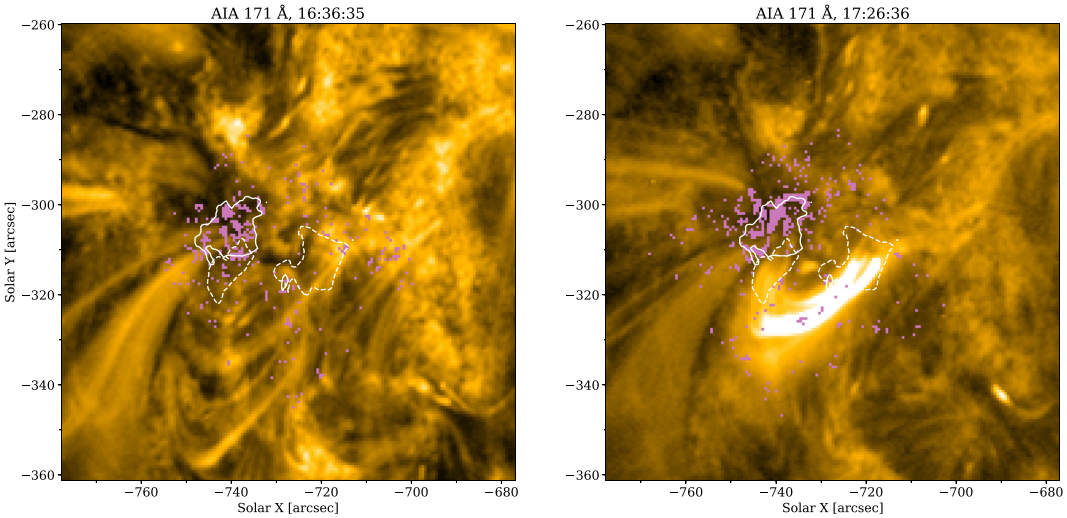

Figure 16. Images from the 171 Å passband from AIA from before (left) and after (right) the flare. The colour scales of the images are different, for the best contrast. Plotted in pink are the locations of macropixels with spectra which produced Gaussian bumps in the Ca II 8542–0.2 Å results. The solid contours outline the sunspot umbra, using the 40 per cent intensity level of the line wing, and the dashed contours show the flare ribbons, determined by 55 per cent of the maximum intensity value of 8542 Å core at the start of the post-impulsive period.

lack of signals at the locations of the chromospheric flare ribbons, perhaps due to the intense heating of the plasma at these locations. Significant magnetic field changes in HMI data were observed at some other locations where the oscillatory behaviour disappeared after the flare activity. In both pre-flare and post-impulsive results, the periods at which the oscillations were observed increases radially out from the umbra, but in post-impulsive data the periods are in general longer.

We believe these results are evidence of a changed magnetic environment in the sunspot as a result of the flare activity, and this interpretation is supported by sudden field changes observed by HMI and by images of coronal loops which are connected to the site. Our work provides evidence of the ways solar flares can affect the solar atmosphere, in particular the chromosphere, and that the flare's influence can be felt over the whole active region.

ACKNOWLEDGEMENTS

The authors would like to thank the anonymous referee for their helpful comments. DCLM would like to thank the Carnegie Trust for the Universities of Scotland for support through PhD scholarship PHD007733, and Sam Grant and James Threlfall for insightful conversations. LF is grateful for support from UK Research and Innovation's Science and Technology Facilities Council under grant award numbers ST/P000533/1 and ST/T000422/1. The research leading to these results has received funding from the European Community's Seventh Framework Programme (FP7/2007–2013) under grant agreement no. 606862 (F-CHROMA). ROM would like to thank the Science and Technologies Facilities Council (UK) for the award of an Ernest Rutherford Fellowship (ST/N004981/1).

DATA AVAILABILITY STATEMENT

The CRISP data which were analysed in this study are available on the F-CHROMA database (f-chroma.org). The SDO data can be accessed from the Joint Science Operations Centre (jsoc.stanford.edu). Scripts used to generate these results and the figures in this paper can be found at github.com/davidclmillar.

REFERENCES

Aschwanden M. J., 2011, Sol. Phys., 274, 99
Aschwanden M. J., Fletcher L., Schrijver C. J., Alexander D., 1999, ApJ, 520, 880
Auchère F., Froment C., Bocchialini K., Buchlin E., Solomon J., 2016, ApJ, 825, 110
Battams K., Gallagher B. M., Weigel R. S., 2019, Sol. Phys., 294, 11
Bel N., Leroy B., 1977, A&A, 55, 239
Bhatnagar A., Tanaka K., 1972, Sol. Phys., 24, 87
Dolla L. et al., 2012, ApJ, 749, L16
Fleck B., Schmitz F., 1991, A&A, 250, 235
Hoeksema J. T. et al., 2014, Sol. Phys., 289, 3483
Inglis A. R., Ireland J., Dominique M., 2015, ApJ, 798, 11
Inglis A. R., Nakariakov V. M., 2009, A&A, 493, 259
Jess D. B., Reznikova V. E., Van Doorsselaere T., Keys P. H., Mackay D. H., 2013, ApJ, 779, 168
Khomenko E., Collados M., 2015, Living Rev. Sol. Phys., 12, 6
Kleint L., 2017, ApJ, 834, 26
Kobanov N. I., Kolobov D. Y., Chupin S. A., 2008, Astron. Lett., 34, 133
Kobanov N. I., Kolobov D. Y., Chupin S. A., Nakariakov V. M., 2011, A&A, 525, A41
Kosovichev A. G., Sekii T., 2007, ApJ, 670, L147
Kuridze D., Mathioudakis M., Simoes P. J. A., 2015, ApJ, 813, 9
Kwak H., Chae J., Song D., Kim Y.-H., Lim E.-K., Madjarska M. S., 2016, ApJ, 821, L30
Lamb H., 1909, Proc. London Math. Soc., s2-7, 122
Leibacher J.W., Stein R. F., 1981, in Jordan S.D., eds, The Sun as a Star, NASA Special Publication, SP-450. NASA/ CNRS, Washington DC/ Paris, p. 370
Lemen J. R. et al., 2012, Sol. Phys., 275, 17
Milligan R. O., Fleck B., Ireland J., Fletcher L., Dennis B. R., 2017, ApJ, 848, L8
Mumford S. et al., 2020, J. Open Source Soft., 5, 1832
Nakariakov V. M., Verwichte E., 2005, Living Rev. Sol. Phys., 2, 3
Pesnell W. D., Thompson B. J., Chamberlin P. C., 2012, Sol. Phys., 275, 3
Petrie G. J. D., 2019, ApJS, 240, 11

Quinn S., Reid A., Mathioudakis M., Nelson C., Krishna Prasad S., Zharkov S., 2019, ApJ, 881, 82
Reznikova V. E., Shibasaki K., Sych R. A., Nakariakov V. M., 2012, ApJ, 746, 119
Rubio da Costa F., Kleint L., Petrosian V., Sainz Dalda A., Liu W., 2015, ApJ, 804, 56
Scharmer G. B., Dettori P. M., Lofdahl M. G., Shand M., 2003, in Keil S. L., Avakyan S. V., eds, Proc. SPIE Conf. Ser. Vol. 4853, Innovative Telescopes and Instrumentation for Solar Astrophysics. SPIE, Bellingham, p. 370
Scharmer G. B. et al., 2008, ApJ, 689, L69
Schou J. et al., 2012, Sol. Phys., 275, 229
Simões P. J. A., Hudson H. S., Fletcher L., 2015, Sol. Stellar Flares, 290, 3625
Simões P. J. A., Reid H. A. S., Milligan R. O., Fletcher L., 2019, ApJ, 870, 114
Sudol J. J., Harvey J. W., 2005, ApJ, 635, 647
Sych R., Nakariakov V. M., Karlicky M., Anfinogentov S., 2009, A&A, 505, 791
Sych R., Zhugzhda Y., Yan X., 2020, ApJ, 888, 84
Threlfall J., De Moortel I., Conlon T., 2017, Sol. Phys., 292, 165
Torrence C., Compo G. P., 1998, Bull. Am. Meteorol. Soc., 79, 61
Van Doorsselaere T., Kupriyanova E. G., Yuan D., 2016, Sol. Phys., 291, 3143
Virtanen P. et al., 2020, Nature Methods, 17, 261

This paper has been typeset from a TEX/LATEX file prepared by the author.

List of astronomical key words (Updated on 2020 January)

This list is common to *Monthly Notices of the Royal Astronomical Society, Astronomy and Astrophysics*, and *The Astrophysical Journal*. In order to ease the search, the key words are subdivided into broad categories. No more than *six* subcategories altogether should be listed for a paper.

The subcategories in boldface containing the word 'individual' are intended for use with specific astronomical objects; these should never be used alone, but always in combination with the most common names for the astronomical objects in question. Note that each object counts as one subcategory within the allowed limit of six.

The parts of the key words in italics are for reference only and should be omitted when the keywords are entered on the manuscript.

General
editorials, notices
errata, addenda
extraterrestrial intelligence
history and philosophy of astronomy
miscellaneous
obituaries, biographies
publications, bibliography
sociology of astronomy
standards

Physical data and processes
acceleration of particles
accretion, accretion discs
asteroseismology
astrobiology
astrochemistry
astroparticle physics
atomic data
atomic processes
black hole physics
chaos
conduction
convection
dense matter
diffusion
dynamo
elementary particles
equation of state
gravitation
gravitational lensing: micro
gravitational lensing: strong
gravitational lensing: weak
gravitational waves
hydrodynamics
instabilities
line: formation
line: identification
line: profiles
magnetic fields
magnetic reconnection
(magnetohydrodynamics) MHD
masers
molecular data
molecular processes
neutrinos
nuclear reactions, nucleosynthesis, abundances
opacity
plasmas
polarization
radiation: dynamics
radiation mechanisms:general
radiation mechanisms: non-thermal
radiation mechanisms: thermal
radiative transfer
relativistic processes
scattering
shock waves
solid state: refractory
solid state: volatile
turbulence
waves

Astronomical instrumentation, methods and techniques
atmospheric effects
balloons
instrumentation: adaptive optics
instrumentation: detectors
instrumentation: high angular resolution
instrumentation: interferometers
instrumentation: miscellaneous
instrumentation: photometers
instrumentation: polarimeters
instrumentation: spectrographs
light pollution
methods: analytical
methods: data analysis
methods: laboratory: atomic
methods: laboratory: molecular
methods: laboratory: solid state
methods: miscellaneous
methods: numerical
methods: observational
methods: statistical
site testing
space vehicles
space vehicles: instruments
techniques: high angular resolution
techniques: image processing
techniques: imaging spectroscopy
techniques: interferometric
techniques: miscellaneous
techniques: photometric
techniques: polarimetric
techniques: radar astronomy
techniques: radial velocities
techniques: spectroscopic
telescopes

Astronomical data bases
astronomical data bases: miscellaneous
atlases
catalogues
surveys
virtual observatory tools

Software
software: data analysis
software: development
software: documentation
software: public release
software: simulations

Astrometry and celestial mechanics
astrometry
celestial mechanics
eclipses
ephemerides
occultations
parallaxes
proper motions
reference systems
time

The Sun
Sun: abundances
Sun: activity
Sun: atmosphere
Sun: chromosphere
Sun: corona
Sun: coronal mass ejections (CMEs)
Sun: evolution
Sun: faculae, plages
Sun: filaments, prominences
Sun: flares
Sun: fundamental parameters
Sun: general
Sun: granulation
Sun: helioseismology
Sun: heliosphere
Sun: infrared
Sun: interior
Sun: magnetic fields
Sun: oscillations
Sun: particle emission
Sun: photosphere
Sun: radio radiation
Sun: rotation
(Sun:) solar–terrestrial relations
(Sun:) solar wind
(Sun:) sunspots
Sun: transition region
Sun: UV radiation
Sun: X-rays, gamma-rays

Planetary systems
comets: general

comets: individual: . . .
Earth
interplanetary medium
Kuiper belt: general

Kuiper belt objects: individual: . . .
meteorites, meteors, meteoroids
minor planets, asteroids: general

minor planets, asteroids: individual: . . .
Moon
Oort Cloud
planets and satellites: atmospheres
planets and satellites: aurorae
planets and satellites: composition
planets and satellites: detection
planets and satellites: dynamical evolution and stability
planets and satellites: formation
planets and satellites: fundamental parameters
planets and satellites: gaseous planets
planets and satellites: general

planets and satellites: individual: . . .
planets and satellites: interiors
planets and satellites: magnetic fields
planets and satellites: oceans
planets and satellites: physical evolution
planets and satellites: rings
planets and satellites: surfaces
planets and satellites: tectonics
planets and satellites: terrestrial planets
planet–disc interactions
planet–star interactions
protoplanetary discs
zodiacal dust

Stars
stars: abundances
stars: activity
stars: AGB and post-AGB
stars: atmospheres
(stars:) binaries *(including multiple)*: close
(stars:) binaries: eclipsing
(stars:) binaries: general
(stars:) binaries: spectroscopic
(stars:) binaries: symbiotic
(stars:) binaries: visual
stars: black holes
(stars:) blue stragglers
(stars:) brown dwarfs
stars: carbon
stars: chemically peculiar
stars: chromospheres
(stars:) circumstellar matter
stars: coronae
stars: distances
stars: dwarf novae
stars: early-type
stars: emission-line, Be
stars: evolution
stars: flare
stars: formation
stars: fundamental parameters
(stars:) gamma-ray burst: general
(stars:) **gamma-ray burst: individual: . . .**
stars: general
(stars:) Hertzsprung–Russell and colour–magnitude diagrams
stars: horizontal branch
stars: imaging
stars: individual: . . .
stars: interiors

stars: jets
stars: kinematics and dynamics
stars: late-type
stars: low-mass
stars: luminosity function, mass function
stars: magnetars
stars: magnetic field
stars: massive
stars: mass-loss
stars: neutron
(stars:) novae, cataclysmic variables
stars: oscillations *(including pulsations)*
stars: peculiar *(except chemically peculiar)*
(stars:) planetary systems
stars: Population II
stars: Population III
stars: pre-main-sequence
stars: protostars
(stars:) pulsars: general
(stars:) **pulsars: individual: . . .**
stars: rotation
stars: solar-type
(stars:) starspots
stars: statistics
(stars:) subdwarfs
(stars:) supergiants
(stars:) supernovae: general
(stars:) **supernovae: individual: . . .**
stars: variables: Cepheids
stars: variables: Scuti
stars: variables: general
stars: variables: RR Lyrae
stars: variables: S Doradus
stars: variables: T Tauri, Herbig Ae/Be
(stars:) white dwarfs
stars: winds, outflows
stars: Wolf–Rayet

Interstellar medium (ISM), nebulae
ISM: abundances
ISM: atoms
ISM: bubbles
ISM: clouds
(ISM:) cosmic rays
(ISM:) dust, extinction
ISM: evolution
ISM: general
(ISM:) HII regions
(ISM:) Herbig–Haro objects

ISM: individual objects: . . .
(except planetary nebulae)
ISM: jets and outflows
ISM: kinematics and dynamics
ISM: lines and bands
ISM: magnetic fields
ISM: molecules
(ISM:) photodissociation region (PDR)
(ISM:) planetary nebulae: general
(ISM:) **planetary nebulae: individual: . . .**
ISM: structure
ISM: supernova remnants

The Galaxy
Galaxy: abundances
Galaxy: bulge
Galaxy: centre
Galaxy: disc
Galaxy: evolution
Galaxy: formation
Galaxy: fundamental parameters
Galaxy: general
(Galaxy:) globular clusters: general
(Galaxy:) **globular clusters: individual: . . .**
Galaxy: halo
Galaxy: kinematics and dynamics
(Galaxy:) local interstellar matter
Galaxy: nucleus
(Galaxy:) open clusters and associations: general
(Galaxy:) **open clusters and associations: individual: . . .**
(Galaxy:) solar neighbourhood
Galaxy: stellar content
Galaxy: structure

Galaxies
galaxies: abundances
galaxies: active
galaxies: bar
(galaxies:) BL Lacertae objects: general
(galaxies:) **BL Lacertae objects: individual: . . .**
galaxies: bulges
galaxies: clusters: general

galaxies: clusters: individual: . . .
galaxies: clusters: intracluster medium
galaxies: disc
galaxies: distances and redshifts
galaxies: dwarf
galaxies: elliptical and lenticular, cD
galaxies: evolution
galaxies: formation
galaxies: fundamental parameters
galaxies: general
galaxies: groups: general

galaxies: groups: individual: . . .
galaxies: haloes
galaxies: high-redshift

galaxies: individual: . . .
galaxies: interactions
(galaxies:) intergalactic medium
galaxies: irregular
galaxies: ISM
galaxies: jets
galaxies: kinematics and dynamics
(galaxies:) Local Group
galaxies: luminosity function, mass function
(galaxies:) Magellanic Clouds
galaxies: magnetic fields
galaxies: nuclei
galaxies: peculiar
galaxies: photometry
(galaxies:) quasars: absorption lines
(galaxies:) quasars: emission lines
(galaxies:) quasars: general

(galaxies:) **quasars: individual: . . .**
(galaxies:) quasars: supermassive black holes
galaxies: Seyfert
galaxies: spiral
galaxies: starburst
galaxies: star clusters: general

galaxies: star clusters: individual: . . .
galaxies: star formation
galaxies: statistics
galaxies: stellar content
galaxies: structure

Cosmology
(cosmology:) cosmic background radiation
(cosmology:) cosmological parameters
(cosmology:) dark ages, reionization, first stars
(cosmology:) dark energy
(cosmology:) dark matter
(cosmology:) diffuse radiation
(cosmology:) distance scale
(cosmology:) early Universe
(cosmology:) inflation
(cosmology:) large-scale structure of Universe
cosmology: miscellaneous
cosmology: observations
(cosmology:) primordial nucleosynthesis
cosmology: theory

Resolved and unresolved sources as a function of wavelength
gamma-rays: diffuse background
gamma-rays: galaxies
gamma-rays: galaxies: clusters
gamma-rays: general
gamma-rays: ISM
gamma-rays: stars
infrared: diffuse background
infrared: galaxies
infrared: general
infrared: ISM
infrared: planetary systems
infrared: stars
radio continuum: galaxies
radio continuum: general
radio continuum: ISM
radio continuum: planetary systems
radio continuum: stars
radio continuum: transients
radio lines: galaxies
radio lines: general
radio lines: ISM
radio lines: planetary systems
radio lines: stars
submillimetre: diffuse background
submillimetre: galaxies
submillimetre: general
submillimetre: ISM
submillimetre: planetary systems
submillimetre: stars
ultraviolet: galaxies
ultraviolet: general
ultraviolet: ISM
ultraviolet: planetary systems
ultraviolet: stars
X-rays: binaries
X-rays: bursts
X-rays: diffuse background
X-rays: galaxies
X-rays: galaxies: clusters
X-rays: general
X-rays: individual: . . .
X-rays: ISM
X-rays: stars

Transients
(transients:) black hole mergers
(transients:) black hole - neutron star mergers
(transients:) fast radio bursts
(transients:) gamma-ray bursts
(transients:) neutron star mergers
transients: novae
transients: supernovae
transients: tidal disruption events